Upscaling of Modeling of Thermal Dispersion in Stratified Geothermal Formations

Tang, Jinyu; Wang, Yang; Rossen, William R.

DOI
10.2118/216904-MS

Publication date
2023

Document Version
Final published version

Published in
Society of Petroleum Engineers - ADIPEC, ADIP 2023

SPE International
Society of Petroleum Engineers

SPE-216904-MS

Upscaling of Modeling of Thermal Dispersion in Stratified Geothermal Formations

Jinyu Tang, Department of Chemical and Petroleum Engineering, United Arab Emirates University, Al Ain, Abu Dhabi, United Arab Emirates; Yang Wang, Department of Civil Engineering, Qingdao University of Technology, Qingdao, China; William R. Rossen, Department of Geoscience and Engineering, Delft University of Technology, Delft, the Netherlands

This paper was prepared for presentation at the ADIPEC held in Abu Dhabi, UAE, 2 – 5 October, 2023.

Abstract

Upscaling of geothermal properties is necessary given the computational cost of numerical simulations. Nevertheless, accurate upscaling of thermo-physical properties of layers combined in simulation grid blocks has been a long-standing challenge. In stratified porous media, non-uniform velocity between layers combined with transverse thermal conduction across layers causes spreading of the thermal front: thermal Taylor dispersion. Neither effect of heterogeneity is accounted for in conventional upscaling. Based on thermal Taylor dispersion, we develop a new upscaling technique for simulation of geothermal processes in stratified formations. In particular, we derive a model for effective longitudinal thermal diffusivity in the direction of flow, α_{eff}, to represent this phenomenon in two-layer media. α_{eff}, accounting for differences in velocity and transverse thermal conduction, is much greater than the thermal diffusivity of the rock itself, leading to a remarkably larger effective dispersion. We define a dimensionless number, N_{TC}, a ratio of times for longitudinal convection to transverse conduction, as an indicator transverse thermal equilibration of the system during cold-water injection. Both N_{TC} and α_{eff} equations are verified by a match to numerical solutions for convection/conduction in two-layer systems. We find that for $N_{TC} > 5$, thermal dispersion in the system behaves as a single layer with α_{eff} This suggests a two-layer medium satisfying $N_{TC} > 5$ can be combined into a single layer with an effective longitudinal thermal diffusivity α_{eff}. Compared with conventional approaches by averaging, the α_{eff} model provides more accurate upscaling of thermal diffusivity and thus more-accurate prediction of cooling-front breakthrough. In stratified geothermal reservoirs with a sequence of layers, upscaling can be conducted in stages, e.g. combining two layers satisfying the N_{TC} criterion in each stage. The application of the new technique to upscaling geothermal well-log data will be presented in a companion paper.

Introduction

Geothermal formations usually feature strong heterogeneity (Blank et al., 2021; Crooijmans et al., 2016). In numerical simulations of geothermal processes, a full description of fine-scale heterogeneity using fine-grid resolution is computationally expensive. It is necessary to upscale the description of formation heterogeneity (Nissen et al., 2018; Rühaak et al., 2015; Vasilyeva et al., 2019), utilizing large grid blocks and assigning uniform properties within each grid block. Conventional upscaling uses arithmetic or volumetric averages of geophysical properties within a grid block (Plumb & Whitaker, 1988). This way of upscaling is often problematic, because fine-scale heterogeneity strongly affects thermal dispersion but is not accounted for in the upscaling. This leads to inaccurate prediction of thermal breakthrough. Our goal is to develop a more-effective approach for upscaling: specifically, of thermo-physical properties of rocks, accounting for the effect of fine-scale heterogeneity of layers combined within simulation grid blocks.

Taylor (1953) analyzed the concentration distribution of solute in liquid fluid flowing slowly through a tube. The spreading of the concentration distribution results from combined effects of convection and longitudinal and transverse diffusion (Dentz et al., 2018; Taylor, 1953). The transverse diffusion arises from velocity variations in the vertical cross-section, as shown in Fig. 1a., shrinking the concentration spreading that would result from convection alone. This phenomenon is known as Taylor dispersion. It has been extensively studied in various bulk and subsurface processes, e.g. transport of contaminant or radioactive waste (Barton, 1983; Berkowitz & Scher, 1996; Detwiler et al., 2002; Shin et al., 2020; Yeo & Ge, 2001), mixing of oil-displacing agents (Dejam, 2019; Lake & Hirasaki, 1981), or dispersion of a tracer (Horne & Rodriguez, 1983; Hinton & Woods, 2020). The spreading of solute concentration in the flow direction is dominated by Taylor dispersion from non-uniform convection and transverse diffusion across streamlines. John et al. (2010) also illustrate that for field-scale mixing in heterogeneous formations, velocity variation between layers together with transverse diffusion across layers is primarily dominant over longitudinal diffusion. This indicates that ignoring longitudinal diffusion may cause little or no loss of accuracy in the modeling of dispersion.

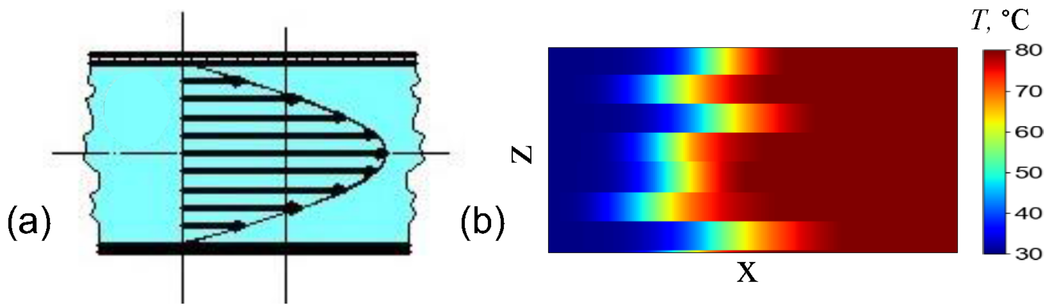

Figure 1—(a) – Fluid-velocity profile in cross-section during fluid flow through a pipe (adapted from Wikipedia (2016)) and (b) Non-even cooling fronts between layers upon cold-water injection into a hot-water-saturated multi-layer porous medium (Nieuwkerk, 2022).

Thermal dispersion in stratified geothermal formations exhibits a similar phenomenon: velocity variations between layers result in non-uniform thermal fronts, illustrated in Fig. 1b. This causes transverse thermal conduction across layers, which reduces the spreading of the cooling front: thermal Taylor dispersion (Bruderer & Bernabé, 2001; Emami Meybodi & Hassanzadeh, 2011; Yan et al., 2022). In effect, thermal Taylor dispersion slows down the advance of the leading edge of the cooling front. This is especially crucial in that the advance of the cooling front dominates the thermal lifetime of a geothermal process and thus production of geothermal energy.

This phenomenon has been addressed in various thermal processes, e.g. wellbore heat transmission in the petroleum industry or transportation of geothermal fluids for heating (Batycky et al., 1994; Hasan & Kabir, 1994; Ortan et al., 2009; Park et al., 2018; Ramey, 1962; Tang & van der Zee, 2021). In these processes, the major cause is velocity variation within a pipe or channel (e.g., Kvernvold & Tyvand, 1980; Nakayama et al., 2006; Pearce & Daou, 2014). However, no model has yet accounted for Taylor dispersion of the temperature front in vertically heterogeneous porous media.

We investigate the effect of heterogeneity within a geothermal reservoir on thermal dispersion (Bredesen et al. 2020; Seibert et al., 2014; Wang et al., 2020). Heat conduction from the overburden and underburden affects the advance of the thermal front inside a reservoir (Willems et al., 2017), but is neglected for simplification. The approach we deploy is similar to that of Lake and Hiraski (1981) for chemical dispersion. Nevertheless, heat conduction is different from chemical diffusion, especially in that heat conduction is through both fluid and surrounding rocks and its dispersion coefficient is of order ~ 10^{-6} m^2/s, about 10^3 times greater than chemical-diffusion coefficient of liquids (~ 10^{-9} m^2/s). Our goals are (1) to define the measure of the effects of transverse thermal conduction and (2) represent thermal Taylor dispersion in layered porous media using an effective thermal diffusivity in a two-layer porous medium. In particular, based on a two-layer geological model, we define and validate a dimensionless criterion for when thermal dispersion in a two-layer heterogeneous medium behaves as a single-homogeneous layer. An analytical model for effective longitudinal thermal diffusivity is then developed and verified to represent the effective dispersion in the system. This model can be applied to upscaling stratified geothermal reservoirs, e.g. by carrying out such upscaling in multiple stages (two layers per stage) to produce properties of a single simulation grid block that combines multiple layers. We outline the general approach for the use of the N_{TC} and α_{eff} model to upscale geothermal well-log data in heterogeneous formations. Specific procedures and illustration for its effectiveness will be presented in a companion study (Nieuwkerk, 2022).

Geological Model, Assumptions and Definitions

Two-layer Geological Model

Figure 2a shows the well-log data from a geothermal reservoir featuring a pattern of layers. The thermal Taylor dispersion theory for upscaling is developed based on a two-layer system that represents such a sequence, as shown in Fig. 2b. The theory is derived for two representative scenarios: (1) two permeable layers with a permeability contrast and (2) two layers with one layer impermeable.

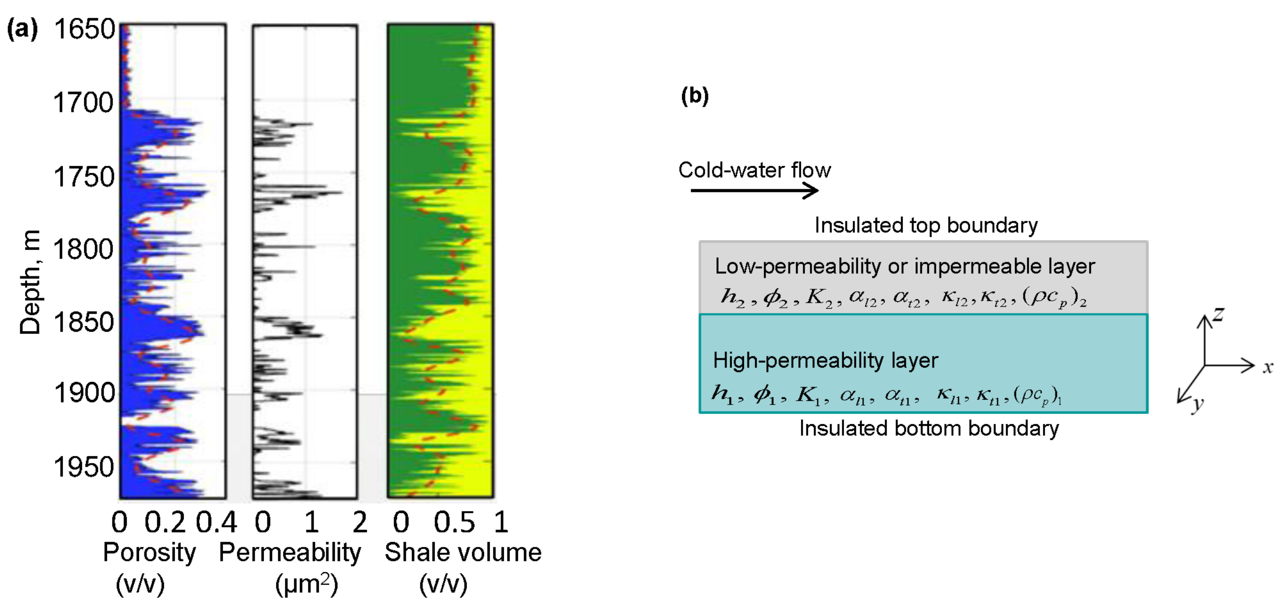

Figure 2—Geothermal formations featuring interspersed layers: (a) well-log data (Bredesen et al., 2020) and (b) a two-layer model.

Each layer j = 1 or 2 is characterized by the properties: h_j – thickness in the z direction, ϕ_j – porosity, K_j – permeability, and α_{lj} and α_{tj} – longitudinal and transverse thermal diffusivity. Respectively, α_{lj} and α_{tj} are ratios of thermal conductivity in the given direction to heat capacity, i.e., [$\kappa_{lj} /(\rho cp)_j$] and [$\kappa_{tj} /(\rho cp)_j$] with j =1 denoting the higher-permeability layer.

Assumptions and Definitions

For the analysis of thermal Taylor dispersion, we have made the following simplifying assumptions:

- Single-phase, incompressible flow with uniform and constant fluid density and viscosity (no phase changes). As a result, there is no crossflow between layers.
- Uniform layer width in the third (y) dimension.
- On the pore scale, local thermal equilibrium, i.e. immediate thermal equilibration between fluid and surrounding rock grains.
- Perfectly insulated top and bottom boundaries.

Dimensionless Variables. To facilitate the problem description, we deploy dimensionless variables:

$$\left.\begin{aligned} T_D &= \frac{T_{inj}-T}{T_{inj}-T_{ini}} \\ x_D &= \frac{x}{L} \\ z_D &= \frac{z}{H} \\ Q_D &= \frac{\bar{v}t}{L} \end{aligned}\right\}, \tag{1}$$

where T_D is the dimensionless temperature with temperature T normalized with respect to injection (T_{inj}) and initial (T_{ini}) temperature; x_D and Z_D are the dimensionless horizontal and vertical positions, with coordinates x and z normalized by reservoir length L and total thickness H, respectively; Q_D is the dimensionless time, representing the total heat capacity of the fluid volume injected at time t divided by the heat capacity of the two-layer medium. $\bar{v}$ in Q_D is the average velocity of the cooling-front in the two-layer system, which is given below.

Cooling-front Velocity. The volumetric heat capacity of layer j is the volume-weighted average of water ($\rho_w cpw$) and rock grain ($\rho_{gi} c_{pgj}$) heat capacities:

$$\left(\rho c_p\right)_j = \varphi_j \rho_w c_{pw} + \left(1-\varphi_j\right)\rho_{gj} c_{pgj}. \tag{2}$$

The average heat capacity of the two-layer system is the thickness-weighted average:

$$\overline{\left(\rho c_p\right)} = \frac{\left(\rho c_p\right)_1 h_1 + \left(\rho c_p\right)_2 h_2}{H}. \tag{3}$$

Assuming local thermal equilibrium (i.e. instantaneous thermal equilibration between fluid and rock grains through which it flows) and no dispersion between cold and hot regions within layers or conduction between layers, T_D at the cooling front is a unit step change in each layer. We define a control volume of dimensions ($Wh_j\Delta x$) just ahead of this front, where W is the reservoir thickness in the y direction (Fig. 2b). The front advances through this volume in time Δt. An energy balance on this volume gives the velocity of the cooling front in each layer j:

$$v_j = \frac{\Delta x}{\Delta t} = \frac{u_j \rho_w c_{pw}}{\varphi_j \rho_w c_{pw} + \left(1-\varphi_j\right)\rho_{gj} c_{pgj}} = \frac{u_j \rho_w c_{pw}}{\left(\rho c_p\right)_j}, \tag{4}$$

where u_j is the Darcy velocity in layer j.

The pore velocity of fluid is (u_j/ϕ_j). v_j in Eq. 4 is proportional to the fluid pore velocity (u_j/ϕ_j), but slowed down by a heat-capacity ratio of the fluid to fluid-matrix combination, [$(\rho_w c_{pw})\phi_j/(\rho c_p)j$]. This delay is known as the retardation effect (Oldenburg & Pruess, 1998).

Assuming instantaneous thermal equilibration across the layers and no dispersion in the flow (x) direction gives the thermal-front velocity, $\bar{v}$, i.e. heat capacity-thickness weighted average:

$$\bar{v} = \frac{\Delta x}{\Delta t} = \frac{u_1 \rho_w c_{pw} h_1 + u_2 \rho_w c_{pw} h_2}{\left[\varphi_1 \rho_w c_{pw} + \left(1-\varphi_1\right)\rho_{g1} c_{pg1}\right] h_1 + \left[\varphi_2 \rho_w c_{pw} + \left(1-\varphi_2\right)\rho_{g2} c_{pg2}\right] h_2} = \frac{v_1 \left(\rho c_p\right)_1 h_1 + v_2 \left(\rho c_p\right)_2 h_2}{\left(\rho c_p\right)_1 h_1 + \left(\rho c_p\right)_2 h_2}. \tag{5}$$

The heterogeneity of the system in Fig. 2b is characterized by the following factors:

$F_h \equiv \dfrac{h_1}{H}$: Fraction of total thickness in the high-permeability layer

$F_c \equiv \dfrac{\left(\rho c_p\right)_1}{\left(\rho c_p\right)_2}$: Heat-capacity contrast between layers

$F_K \equiv \dfrac{K_1}{K_2}$: Permeability contrast between layers

For the scenario with two permeable layers, Eqs. 4 and 5, incorporating Darcy's Law for u_j, yield the following velocity correlations:

$$\left.\begin{aligned} \frac{v_1}{v_2} &= \frac{F_K}{F_c} \\ \frac{v_1}{\bar{v}} &= \frac{\left(F_{ch}+1\right)F_K}{F_K F_{ch}+F_c} \\ \frac{v_2}{\bar{v}} &= \frac{\left(F_{ch}+1\right)F_c}{F_K F_{ch}+F_c} \end{aligned}\right\}, \tag{6}$$

Equations 2 and 3 give the heat-capacity relations:

$$\left.\begin{aligned} \frac{\left(\rho c_p\right)_1}{\left(\overline{\rho c_p}\right)} &= \frac{F_c}{F_c F_h + \left(1-F_h\right)} \\ \frac{\left(\rho c_p\right)_2}{\left(\overline{\rho c_p}\right)} &= \frac{1}{F_c F_h + \left(1-F_h\right)} \end{aligned}\right\}. \tag{7}$$

For the scenario with one layer impermeable, i.e. $K_2 = 0$, the heat-capacity relations in Eq. 7 still hold. Nevertheless, as $v_2 = 0$, the velocity relations in Eq. 6 become

$$\left.\begin{aligned} \frac{v_1}{\bar{v}} &= \frac{F_{ch}+1}{F_{ch}} \\ \frac{v_2}{\bar{v}} &= 0 \end{aligned}\right\}. \tag{8}$$

Definition of Transverse Thermal-Conduction Number N_{TC}

The thermal lifetime of a geothermal process is usually dominated by pressure-driven convection. Nevertheless, it is strongly affected by thermal conduction, in particular conduction in the transverse direction arising from unequal cooling-front velocities in the two layers. Such transverse conduction has a significant effect on the advance of the cooling front, affecting the breakthrough of cold water and thus process lifetime. As a measure of the transverse thermal conduction relative to convection, we define a dimensionless number N_{TC}, a time ratio given by

$$N_{TC} \equiv \frac{t_{lj}}{t_{tj}} = \frac{L}{H} \frac{e_{tj}}{e_{lj}}, \tag{9}$$

where

t_{lj}: convection-driven thermal-front breakthrough time in layer j;

t_{tj}: transverse thermal-conduction time across the two layers;

(e_{tj}/e_{lj}): ratio of heat fluxes driven by transverse conduction and longitudinal convection:

$$e_{l\,j} = v_j T, \tag{10}$$

$$e_{t\,j} = -\left(\frac{\alpha_{t\,j}}{H}\right)\cdot\left(\frac{\Delta T}{\Delta z_D}\right). \tag{11}$$

Substituting Eqs. 10 and 11 into Eq. 9 yields

$$N_{TC} = \frac{L}{H^2}\frac{\alpha_{t\,j}}{v_j}\left(\frac{-\Delta T/\Delta z_D}{T}\right). \tag{12}$$

Following Lake and Hirasaki (1981), we take [(-$\Delta T/\Delta z_D$)/T in Eq. 12 to be a constant, 12.5 and choose properties making N_{TC} minimum. N_{TC} is the minimum of the following two expressions:

$$\begin{aligned} N_{TC} &= 12.5\times\frac{L}{H^2}\frac{\alpha_{t2}}{v_1}, \\ &= 12.5\times\frac{L}{H^2}\frac{\alpha_{t1}}{v_1}. \end{aligned} \tag{13}$$

The reason for the choice of the factor 12.5 is given below in the verification of the definition of N_{TC}; compare the 12.5 in Eq. 13 for heat conduction with 14 in Lake and Hirasaki and 14.44 in Taylor (1953) for solute transport. The verification of the factor 12.5 in the definition of N_{TC} given below is based on cases with a wide variety of layer geometries with the same initial and injection temperatures. It is possible that an application with a very-different ratio of absolute temperatures might require an adjustment of this value. Greater values of N_{TC} mean either slower convection or faster conduction. Both suggest a larger proportion of the system is at transverse thermal equilibrium during cold-water injection.

Derivation of Effective Longitudinal Thermal Diffusivity - α_{eff}

The detailed derivation of the effective longitudinal thermal diffusivity, α_{eff}, is shown below for the scenario with two layers, both permeable. The scenario with an impermeable layer follows the same procedures.

With the assumptions in the Section 2.2, the energy-balance equation for an infinitesimal volume element in the 2D system of Fig. 2b is

$$\frac{\partial T}{\partial t} + v_j\frac{\partial T}{\partial x} - \alpha_{l\,j}\frac{\partial^2 T}{\partial x^2} - \alpha_{t\,j}\frac{\partial^2 T}{\partial z^2} = 0, \tag{14}$$

where j denotes layer 1 or 2. v_j is given in Eq. 4, which varies in cross-section as a function of layer index j, i.e. again the cause for thermal Taylor dispersion. We transform x to dimensionless coordinate $\hat{x}_D$:

$$\hat{x}_D = \frac{x}{L} - \frac{\bar{v}t}{L} = x_D - Q_D, \tag{15}$$

which is the position relative to a vertical plane moving at velocity $\bar{v}$.

When transverse thermal conduction is significant, i.e. at large values of N_{TC}, the cooling front spreads slowly around the position ($\bar{v}t$) (e.g., Taylor (1956)), suggesting that in the equation recast in terms of $\hat{x}_D$ the term ($\partial T/\partial t$) in Eq. 14 is small and can be neglected: conduction/dispersion around the front spreads like the square root of time and slows down with time. Following Taylor's resu lt and implications of previous work on dispersion in heterogeneous media, we leave out axial heat conduction for simplicity. This simplification gives an equivalent diffusion coefficient representing non-uniform convection and transverse conduction between layers. Eq. 14, inserting dimensionless variables $\hat{x}_D$ and z_D, then becomes:

$$\left(\frac{v_j}{\bar{v}} - 1\right)\frac{\partial T_D}{\partial \hat{x}_D} = \left(\frac{L}{H}\right)^2\frac{\partial}{\partial z_D}\left(\frac{\alpha_{t\,j}}{\bar{v}L}\frac{\partial T}{\partial z_D}\right). \tag{16}$$

Hereafter, the term $(\partial T_D/\partial \hat{x}_D)$ is treated as independent of z_D; this treatment is justified by the fact that significant transverse conduction almost equalizes temperature in the z direction at position $\hat{x}_D$. At boundaries z_D = 0 and 1, heat flux is zero. We integrate both sides of Eq. 16 with respect to z_D, over [0,

z_D] for $0 \leq z_D < F_h$ (layer $j = 1$) and over [z_D, 1| for $F_h \leq z_D \leq 1$ (layer $j = 2$), respectively. Performing a second integration, over [0, z_D] for $0 \leq z_D < F_h$ and over [F_h, z_D| for $F_h \leq z_D \leq 1$, yields the transverse T_D profile as a function of z_D:

for $0 \leq z_D < F_h$:

$$T_D = T_D\Big|_{z_D=0} + \frac{1}{2}\left(\frac{\bar{v}L}{\alpha_{t1}}\right)\left(\frac{H}{L}\right)^2\left(\frac{v_1}{\bar{v}} - 1\right)\left(z_D^2\right)\left(\frac{\partial T_D}{\partial \hat{x}_D}\right), \tag{17}$$

for $F_h \leq z_D \leq 1$:

$$\begin{aligned} T_D = T_D\Big|_{z_D=0} &+ \frac{1}{2}\left(\frac{\bar{v}L}{\alpha_{t1}}\right)\left(\frac{H}{L}\right)^2\left(\frac{v_1}{\bar{v}} - 1\right)\left(F_h^2\right)\left(\frac{\partial T_D}{\partial \hat{x}_D}\right) \\ &+ \frac{1}{2}\left(\frac{\bar{v}L}{\alpha_{t2}}\right)\left(\frac{H}{L}\right)^2\left(\frac{v_2}{\bar{v}} - 1\right)\left(z_D^2 - 2z_D - F_h^2 + 2F_h\right)\left(\frac{\partial T_D}{\partial \hat{x}_D}\right), \end{aligned} \tag{18}$$

where T_D in Eqs. 17 and 18 is equal at $z_D = F_h$, maintaining a continuous heat flux across the layer boundary.

Based on the transverse T_D (z_D) profile, one can solve for the convective heat flux, e_c across the moving plane at $\bar{v}t$, through the following integration:

$$\begin{aligned} e_c &= WH\int_0^1 \left(v_j - \bar{v}\right)\left(\rho c_p\right)_j T_D dz_D \\ &= WH\int_0^{F_h} \left(v_1 - \bar{v}\right)\left(\rho c_p\right)_1 T_D dz_D + WH\int_{F_h}^1 \left(v_2 - \bar{v}\right)\left(\rho c_p\right)_2 T_D dz_D. \end{aligned} \tag{19}$$

e_c is determined by substituting T_D in Eqs. 17 and 18 into the corresponding integral in Eq. 19. With the relations in Eqs. 6 and 7, the expression for e_c is derived as follows:

$$e_c = -\frac{WH\bar{v}\left(\overline{\rho c_p}\right)}{3}\left(\frac{H}{L}\right)^2\left(\frac{F_cF_h}{F_cF_h + 1 - F_h}\right)\left(\frac{F_K - F_c}{F_KF_{ch} + F_c}\right)^2\left[\left(\frac{\bar{v}L}{\alpha_{t1}}\right)F_h^2 + \left(\frac{\bar{v}L}{\alpha_{t2}}\right)F_cF_h\left(1 - F_h\right)\right]\left(\frac{\partial T_D}{\partial \hat{x}_D}\right) + \omega, \tag{20}$$

where ω is a collection of terms independent of $\hat{x}_D$ and canceled in the derivative of e_c to $\hat{x}_D$ below.

Within the front of dimension ($WHd\hat{x}_D$), an energy balance over time interval dQ_D yields

$$WH\bar{v}\left(\overline{\rho c_p}\right)\frac{\partial \tilde{T}_D}{\partial Q_D} + \frac{\partial e_c}{\partial \hat{x}_D} = 0, \tag{21}$$

where $\tilde{T}_D$ is the average temperature in cross-section at $\hat{x}_D$ which is approximately T_D when thermal equilibration across z_D is nearly instantaneous (i.e. at large values of N_{TC}). Solving for the derivative of e_c in Eq. 20 with respect to $\hat{x}_D$ and substituting the derivative into Eq. 21 yields

$$\frac{\partial T_D}{\partial Q_D} = \left(N_{pe}\right)^{-1}\frac{\partial^2 T_D}{\partial \hat{x}_D^2}, \tag{22}$$

where $(N_{pe})^{-1}$ is the equivalent inverse Péclet number as contributed by Taylor dispersion:

$$\left(N_{pe}\right)^{-1} = \frac{\bar{v}H^2}{3L}\left(\frac{F_cF_h}{F_cF_h + 1 - F_h}\right)\left(\frac{F_K - F_c}{F_KF_{ch} + F_c}\right)^2\left[\frac{F_h^2}{\alpha_{t1}} + \frac{F_cF_h\left(1 - F_h\right)}{\alpha_{t2}}\right]. \tag{23}$$

The effective longitudinal diffusivity, α_{eff} is the sum of longitudinal diffusivity and extra diffusivity resulting from heterogeneous convection modified by transverse conduction, analogous to solute dispersion (Aris, 1956; Lake & Hirasaki, 1981):

$$\alpha_{eff} = \bar{\alpha}_l + \bar{v}L\left(N_{pe}\right)^{-1}, \tag{24}$$

where $\bar{\alpha}_l$ is the thickness-weighted average of α_{l1} and α_{l2}

Combining Eqs. 23 and 24 yields the analytical model for α_{eff} for the scenario with two permeable layers:

$$\alpha_{eff} = \bar{\alpha}_l + \frac{\bar{v}^2 H^2}{3}\left(\frac{F_c F_h}{F_c F_h + 1 - F_h}\right)\left(\frac{F_K - F_c}{F_K F_{ch} + F_c}\right)^2\left[\frac{F_h^2}{\alpha_{t1}} + \frac{F_c F_h(1 - F_h)}{\alpha_{t2}}\right], \tag{25}$$

where α_{eff} has the units of m^2/s, when the parameters in the equation use standard units. Note that α_{eff} here and in Eq. 26 below is an effective thermal diffusivity accounting for both water and rock. Treating α_{eff} as volume-weighted average of diffusivities of water and rock, one can then calculate back the effective diffusivity of rock from α_{eff}.

For the scenario with an impermeable layer, the derivation of α_{eff} follows the same steps from Eqs. 14 to 25. To account for K_2 being zero, the relations in Eq. 8 should be used in deriving e_c in Eq. 20. The corresponding expression for α_{eff} in this scenario then becomes:

$$\alpha_{eff} = \bar{\alpha}_l + \frac{\bar{v}^2 H^2}{3}\left(\frac{F_c F_h}{F_c F_h + 1 - F_h}\right)\left(\frac{1}{F_{ch}}\right)^2\left[\frac{F_h^2}{\alpha_{t1}} + \frac{F_c F_h(1 - F_h)}{\alpha_{t2}}\right]. \tag{26}$$

Equation 25 or 26 multiplied by $(\overline{\rho c_p})$ in Eq. 3 gives the effective longitudinal thermal conductivity, κ_{eff} Similar to α_{eff}, κ_{eff} in the flow direction is the sum of longitudinal conductivity (i.e. thickness-weighted average of κ_{l1} and κ_{l2}) and extra conductivity resulting from nonuniform convection and transverse conduction. The effective conductivity of rocks can be calculated from κ_{eff}, treated as the volume-weighted average of the conductivities of water and rock.

Verification of the N_{TC} and α_{eff} Model

We verify both the N_{TC} and α_{eff} equations via comparison with 2D numerical solutions of the energy-balance Eq. 14 for T(x, z, t); the $T(x, t)$ reported in the numerical solutions is the thickness-weighted average of T in the vertical cross-section. Simulation results were obtained with DARTS (Delft Advanced Research Terra Simulator) for geothermal processes (see Khait & Voskov (2018) and Wang et al. (2020) for details of the simulator). The mass- and energy-balance equations were numerically solved in a fully implicit manner with properties of the analytical model. In the setup of the numerical model, the reservoir was initially saturated with single-phase water at 80°C and 190 bar. At the injection-well boundary, cold-water at 30°C was injected at a fixed rate, with whole thickness of the reservoir perforated. There is no flux across other boundaries, except at production well, which is perforated all along its length. The assumption of incompressibility and no density change with temperature for both fluid and rock assures that the fluid velocities are identical in the analytical and numerical modeling. In our simulation runs, fine-grid resolution (1 × 1 × 1 m) and a time step of maximum 10 days were utilized to represent actual thermal dispersion with minimized numerical diffusion.

Table 1 lists the layer properties of the media used in simulations, referring to sandstone for the permeable layer and shale for the impermeable layer (properties taken from Lake et al. (2014)). We assume all properties are isotropic within a layer. Table 2 summarizes the simulation results. The operation rates in geothermal fields vary largely due to different formation properties, production rates and project lifespans. The tested injection rates (in Table 2) scale up with reservoir thickness and are within the range of field rates, e.g. 0.7 to 4 m^3/D over a cross-section area of 100 by 1 m^2 (e.g. Bujakowski et al., 2016; Feng et al., 2017; Wang et al., 2021). Table 2 also lists the upscaled thermal conductivity and diffusivity values, which can be much greater than those of the rock itself. For instance, in Case 5, κ_{eff} = 179.02 W/(m.K), nearly 69 times the conductivity of water-sandstone mixture, 2.61 W/(m.k); α_{eff} = 9.30×10^{-5} m^2/s, nearly 81 times the diffusivity of water-sandstone mixture, 1.15×10^{-6} m^2/s. In conventional upscaling without accounting for Taylor dispersion, the upscaled thermo-physical properties are much less than we show here, e.g. close to those of the rocks involved. Due to underestimated thermal conductivity/diffusivity in conventional upscaling, thermal dispersion is underestimated, which would result in overestimation of thermal breakthrough time.

Table 1—Layer properties used for illustrating the validity of N_{TC} and α_{eff} model.

Reserv oir size		Layer 1 properties						Layer 2 properties				Water
L, m	W, m	Φ_1	K_1, m²	$(\rho c_p)_1$, KJ/m³.K	K_1, W/m.k	α_1, m²/s	Φ_2	K_2, m²	$(\rho c_p)_2$, KJ/m³.K	K_2, W/m.K	α_2, m²/s	KJ/m³.K
1000	1	0.19	5×10⁻¹³	2267.73	2.61	1.15×10⁻⁶	0.19	1.25×10⁻¹³	2267.73	2.61	1.15×10⁻⁶	4190
1000	1	0.19	5×10⁻¹³	2267.73	2.61	1.15×10⁻⁶	0	0	1754.19	1.61	0.92×10⁻⁶	4190

Table 2—Numerical simulation results for transverse thermal conduction

Cases*	h_1, m	h_2, m	Q, m³/D	dp, bar	K_{eff}, W/(m.K)	e_{eff}, m²/s	N_{TC}	$(Q_{D0})_{TD=0.5}$	$(Q_D)_{TD=0.5}$	I_{TC}
1	10	2	0.8496	15.03	5.68	2.51×10⁻⁶	57.74	0.875	1.000	1.000
2	10	2	0.4252	7.91	3.52	1.61×10⁻⁶	87.61	0.866	1.000	1.000
3	10	5	0.5315	9.88	10.23	4.89×10⁻⁶	44.86	0.721	1.000	1.000
4	10	10	0.7087	13.16	39.72	1.98×10⁻⁵	18.92	0.564	1.001	1.002
5	10	20	1.0631	19.60	179.02	9.30×10⁻⁵	5.61	0.393	0.944	0.908
6	10	30	1.4174	25.62	433.86	2.30×10⁻⁴	2.37	0.301	0.835	0.763
7	10	40	1.7718	31.33	807.92	4.35×10⁻⁴	1.21	0.244	0.659	0.549
8	10	50	2.1261	36.99	1302.61	7.08×10⁻⁴	0.70	0.205	0.499	0.370
9	10	90	3.5435	60.92	4497.16	2.49×10⁻³	0.15	0.126	0.232	0.122

*In each case, T_{inj} = 30°C and T_{ini} = 80°C, and simulations of Case 1 and Cases 2 – 9 use the first and second row of layer properties in Table 1, respectively. *dp* denotes the overall pressure drop.

Verification of the Transverse Thermal-Conduction Number N_{TC}. To verify the definition of N_{TC} in Eq. 13, a transverse thermal-conduction index is introduced:

$$I_{TC} \equiv \frac{\left(Q_D\right)_{T_D=0.5} - \left(Q_{D0}\right)_{T_D=0.5}}{1-\left(Q_{D0}\right)_{T_D=0.5}}, \tag{27}$$

where $(Q_D)_{TD=0.5}$ and $(Q_{D0})_{TD=0.5}$ (given in Eq. 1) represent the cumulative heat injection at the breakthrough of T_D = 0.5, with and without thermal conduction in either direction, respectively. T_D = 0.5 is chosen as a representation of the cooling-front breakthrough. In the calculations of I_{TC}, $(Q_D)_{TD=0.5}$ (defined in Eq. 1) is obtained from simulations of various two-layer systems in Table 2. $(Q_{D0})_{TD=0.5}$ depends on F_{Kh}. For a system with two permeable layers, it is given by

$$\begin{cases} For\ F_{Kh} > 1 \quad \left(Q_{D0}\right)_{T_D=0.5} = \dfrac{F_K F_{ch} + F_c}{\left(F_{ch}+1\right)F_K} \\ For\ F_{Kh} < 1 \quad \left(Q_{D0}\right)_{T_D=0.5} = \dfrac{F_K F_{ch} + F_c}{\left(F_{ch}+1\right)F_c} \end{cases}. \tag{28}$$

For a system with one impermeable layer, F_{Kh} is always greater than unity and $(Q_{D0})_{TD=0.5}$ is

$$\left(Q_{D0}\right)_{T_D=0.5} = \frac{F_{ch}}{F_{ch}+1}. \tag{29}$$

The value of I_{TC} in Eq. 27 indicates the accuracy of the assumption of instantaneous transverse thermal-equilibration across the two layers, as the cooling front advances. I_{TC} = 1 indicates the assumption is accurate. For I_{TC} = 1, $(Q_D)_{TD=0.5}$ = 1, meaning that the injected heat required is the heat capacity of the whole system, which occurs only when transverse thermal equilibration is approximately instantaneous. I_{TC} = 0 indicates the least vertical thermal equilibration across the two layers. For $I_{TC} = 0$, $(Q_D)_{TD=0.5} = (Q_{D0})_{TD=0.5}$, meaning the injected heat required is that as though with no transverse conduction at all. The behavior of I_{TC} is illustrated by the 2D T distribution with respect to different values of I_{TC}, as shown in Fig. 3. For instance, in Case 2 with top impermeable layer of $h_2 = 2$ m and bottom permeable layer of $h_1 = 10$ m, $I_{TC} = 1$ and instantaneous or fast equilibration across layers yields uniform T in the cross-section. With the thickness of the impermeable layer h_2 increasing, e.g. $h_2 = 20$ m in Case 5 and $h_2 = 90$ m in Case 9 where $I_{TC} = 0.908$ and 0.122, heat conduction is not fast enough to achieve uniform T in the cross-section.

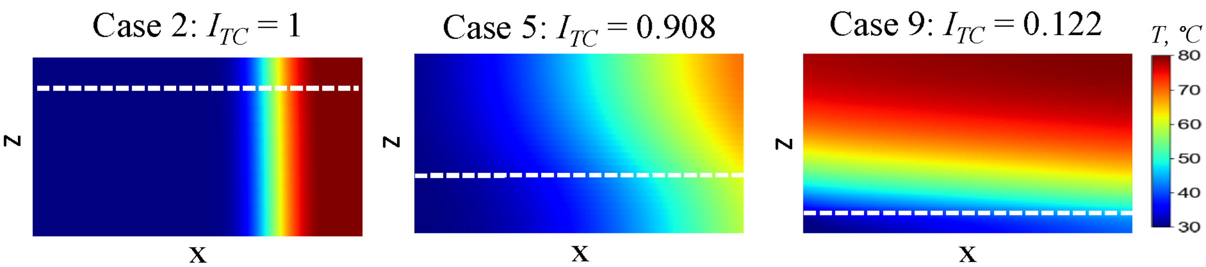

Figure 3—2D temperature (T) distribution at 15 years of cold-water injection in Cases 2, 5 and 9. Dashed line marks layer boundary, with the higher-permeability layer at the bottom in each case.

Figure 4 shows a good correlation between N_{TC} in Eq. 13 and I_{TC} in Eq. 27. For illustration, nine simulations were conducted with respect to different thickness contrasts between the lower-permeability or impermeable layer (h_2) and higher-permeability layer (h_1), as summarized in Table 2. Each simulation run gives a value of I_{TC}, and, based on the layer properties used in the simulation, one can calculate the corresponding value of N_{TC}. With the ratio of (h_2/h_1) increasing from Case 1 to Case 9, it takes longer for transverse conduction across the two layers relative to longitudinal convection, leading to N_{TC} decreasing from 87.61 to 0.15. The longer time required for conduction across the two layers means a smaller fraction of the system is at transverse thermal equilibration, as illustrated in Fig. 3, resulting in I_{TC} decreasing from 1 towards 0. The consistency between N_{TC} and I_{TC} suggests that N_{TC} can be used as an indicator of transverse thermal equilibration of a two-layer medium without running simulations.

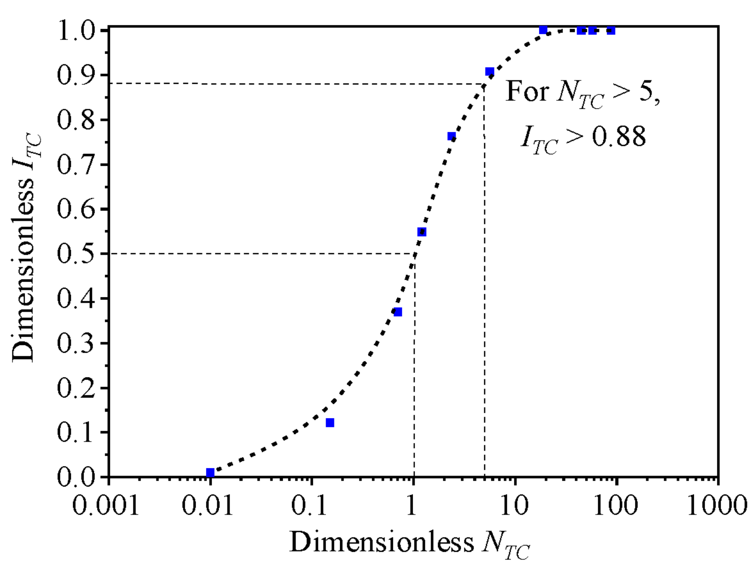

Figure 4—Verification of the transverse thermal-conduction number, N_{TC} (Eq. 13) as an indicator for transverse thermal equilibration, via its correlation with I_{TC} (Eq. 27).

The constant 12.5 in the definition of N_{TC} in Eq. 13 is chosen such that $N_{TC} = 1$ at $I_{TC} = 0.5$, for convenience. For $N_{TC} < 0.01$, I_{TC} is about 0, indicating that a two-layer medium behaves like two layers with no thermal interaction between the layers. For $N_{TC} > 5$, $I_{TC} > 0.88$: the two layers are approaching transverse thermal equilibrium, as shown in Cases 2 and 5 in Fig. 3 and in Fig. 5 in the next section. This further implies, for $N_{TC} > 5$, that thermal dispersion in a two-layer system approximates a single-homogeneous layer. The α_{eff} model in Eqs. 25 or 26 is derived assuming instantaneous thermal equilibration in the cross-section. Therefore, $N_{TC} > 5$ defines a criterion for combining two layers, i.e. also the valid condition for α_{eff} model. The N_{TC} criterion and α_{eff} model is further verified in the next section.

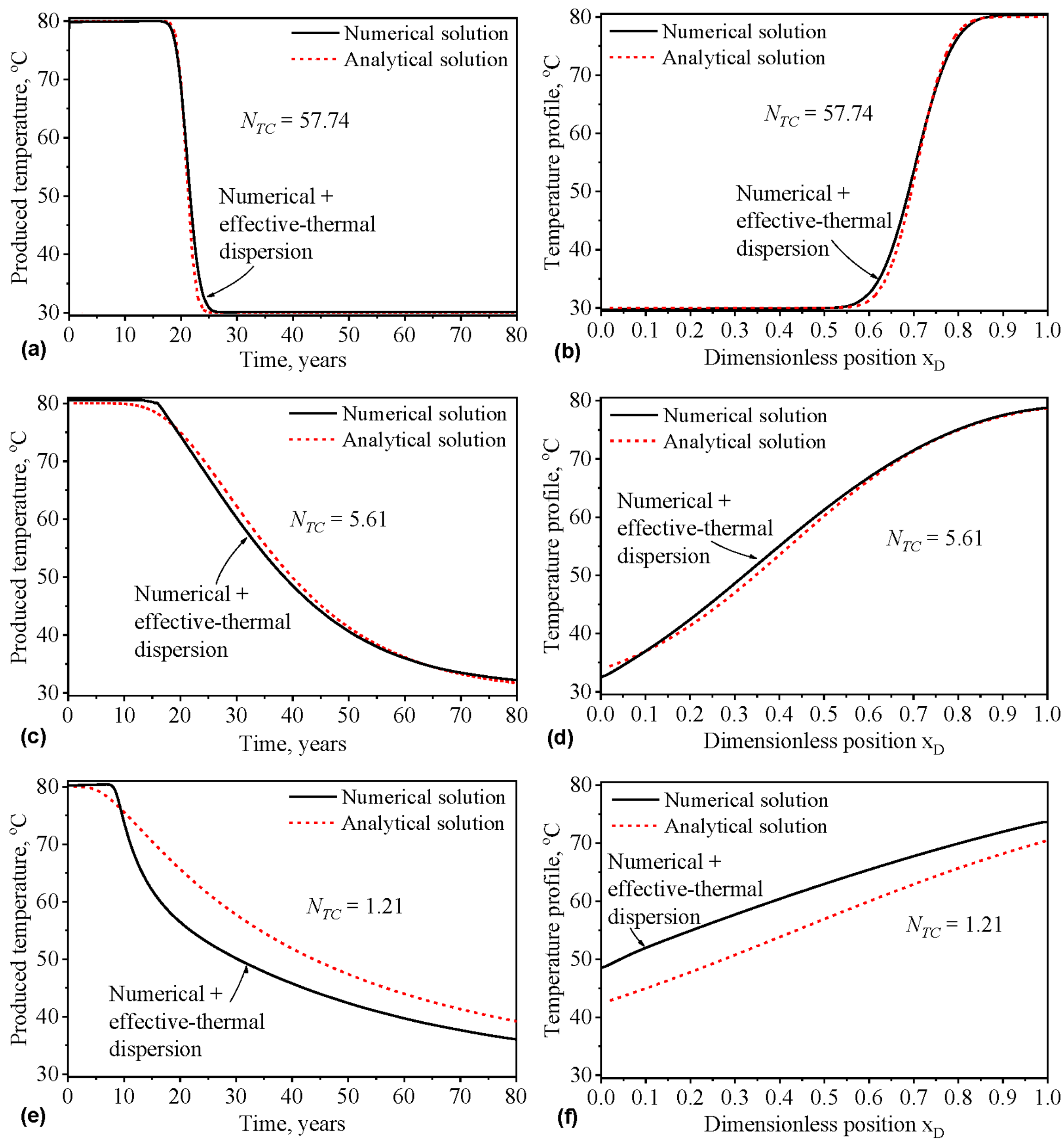

Figure 5—Verification of the α_{eff} model (Eqs. 25 and 26) via comparison with numerical solutions for effluent T history and T profile (at 15 years): (a) and (b) from Case 1; (c) and (d) from Case 5; (e) and (f) from Case 7. See Tables 1 and 2 for simulation details in each case.

Verification of the Effective Longitudinal Thermal-Diffusivity Model α_{eff}. Equation 22 represents the energy-balance equation for a single-layer medium having the average properties of the two-layer system in Fig. 2b. Replacing $(N_{pe})^{-1}$ with the effective inverse Péclet number $(N_{peeff})^{-1}$, an approximate solution to Eq. 22 follows an error function (Axelsson et al., 2005; Gringarten, 1978; Murphy et al., 1981):

$$T_D = 1 - \frac{1}{2}\left[1 - erf\left(\frac{x_D - Q_D}{2\sqrt{Q_D\left(N_{pe}^{eff}\right)^{-1}}}\right)\right], \tag{30}$$

where

$$\left(N_{pe}^{eff}\right)^{-1} \equiv \frac{\alpha_{eff}}{\bar{v}L}. \tag{31}$$

Using Eqs. 30 and 31 and layer properties in Table 1, one can solve analytically for $T(x, t)$ for the combined single-layer medium possessing the average properties of the two layers.

Figure 5 compares the analytical solutions with numerical solutions for both T distribution along x and produced T history, with respect to N_{TC} values. In the numerical solutions, the produced T history reported on the left column in Fig. 5 is a volumetric flow rate-weighted average of produced T from the last column of grid blocks. The T profile reported on the right column in Fig. 5 is a volume-weighted average of T in the vertical column of grid blocks at each position x_D.

In the analytical solutions, α_{eff} in Eq. 25 or 26 is used to represent the effective longitudinal thermal diffusivity in the combined system. For $N_{TC} > 5$, e.g. $NTC = 57.74$ in Case 1 and 5.61 in Case 5, a good match between analytical and numerical solutions is achieved in both effluent T history and T profile. The match verifies the effectiveness of the α_{eff} model for representing thermal Taylor dispersion in a two-layer system, when satisfying the criterion $N_{TC} > 5$. For $N_{TC} < 5$, e.g. $N_{TC} = 1.21$ in Fig. 5e and 5f from Case 7, the fit is not as good. This means that the two layers physically cannot be combined into a single layer or represented by α_{eff}, since transverse conduction is not fast enough to give a uniform T in cross-section.

Implications for Upscaling Simulation of Subsurface Thermal-Dispersion Processes. The concept of effective dispersion can be applied to upscaling the modelling of various subsurface thermal processes, e.g. geothermal processes and thermal enhanced oil recovery. There would also be similarities to dispersion of gas fronts in hydrogen-storage applications, in that the magnitude of gas diffusion coefficients is similar to that of thermal conductivity, though the details of the derivation differ (Lake and Hirasaki, 1981). This suggests that in both applications upscaling is feasible to feasible to a greater extent than with dispersion in liquid flow.

Conventional upscaling approaches use arithmetic or volumetric averaging to estimate dispersion coefficients in layers combined in a simulation grid block. Such averaging does not account for the non-uniform convection modified by transverse conduction between the layers. This underestimates the spreading of dispersion fronts, leading to overestimation of the time to thermal breakthrough (e.g. Babaei and Nick, 2019; Daniilidis et al., 2020). The analytical model α_{eff} accounting for thermal Taylor dispersion provides a more-accurate representation of thermal dispersion in an upscaled system. Below we outline the general approach for extending the N_{TC} layer-combining criterion and α_{eff} model to multi-layer media.

As illustrated in Fig. 5, for $N_{TC} > 5$, thermal dispersion in a two-layer heterogeneous medium approximates a single-layer homogeneous medium. Thus, the definition of N_{TC} provides a physically based criterion for combining two layers, where effective thermal dispersion can be represented by α_{eff}. For a multi-layer reservoir as in Fig. 2a, one can combine layers in stages, two layers each stage. One can calculate the values of N_{TC} for all adjacent pairs of layers and then combine the two layers with maximum N_{TC} (when satisfying the upscaling criterion), and represent the combined group as one layer with thermal diffusivity α_{eff} in the flow direction. The next stage of upscaling will be conducted on the new combined system from the previous stage. This process proceeds until no more adjacent layers satisfy the upscaling criterion. The upscaled description of the reservoir is then used as inputs for thermal-process simulations. In a companion study, we test the validity of the model for upscaling geothermal well-log data with numerous interspersed layers (Nieuwkerk, 2022).

In the derivation of the analytical model for α_{eff}, we exclude some complexities, e.g. heat conduction from overburden and underburden formations, areal heterogeneity and fractures, multi-phase flow, and gravity effects. Further research is needed to understand the effects of these complexities on thermal dispersion in subsurface formations.

Summary and Conclusions

A model for effective longitudinal thermal diffusivity, α_{eff}, is derived from an energy balance, to quantify thermal Taylor dispersion in a two-layer system. α_{eff}, accounting for transverse thermal conduction, can be much greater (e.g., by two orders of magnitude) than the thermal diffusivity of the rock in the formation.

We define a dimensionless number, N_{TC} (i.e. a ratio of times for longitudinal convection and transverse conduction), which can be used as an indicator of transverse thermal equilibration. We find that for $N_{TC} > 5$, thermal dispersion in a two-layer system behaves as a single layer represented by α_{eff}. Thus, the definition of N_{TC} provides a physical criterion for combining two layers.

The approach of upscaling α_{eff} in the flow direction based on the value of N_{TC} is verified by a good match to numerical solutions of the energy-balance equation for thermal convection/conduction in a two-layer system.

The application of the N_{TC} criterion and α_{eff} model to upscaling the description of heterogeneity of stratified geothermal formations will be presented in a companion study.

Acknowledgments

This project is partly funded by the United Arab Emirates University Research Grant (Grant Number: 12N099). The authors acknowledge the insightful discussions and comments by Prof. L. W. Lake of the University of Texas at Austin and Dr. D. Voskov of the Delft University of Technology. T. Griendt, a B.Sc. thesis student at the Delft University of Technology, is gratefully thanked for his preliminary work in this project.

Nomenclature

e_c = heat flux in the flow direction by transverse conduction, J/(s.K)
(e_{tj}/e_{lj}) = ratio of heat fluxes driven by transverse conduction and longitudinal convection, dimensionless (Eqs. 10 and 11)
F_h = fraction of total thickness in the high-permeability layer
F_c = heat-capacity contrast between layers
F_{ch} = heat capacity-thickness contrast between layers
F_k = permeability contrast between layers
H = total reservoir thickness in z direction, m
h_j = layer thickness in z direction, m
I_{TC} = transverse thermal-conduction index, dimensionless (Eq. 27)
j = layer index
K_j = permeability, m^2
L = reservoir length, m
N_{TC} = transverse thermal conduction number, dimensionless (Eq. 13)
$(N_{pe})^{-1}$ = inverse Péclet number, dimensionless (Eq. 23)
$(N_{peeff})^{-1}$ = effective inverse Péclet number, dimensionless (Eq. 31)
Q_D = dimensionless injection time (Eq. 1)

$(Q_{D0})_{TD=0.5}$ = cumulative heat injection at the breakthrough of $T_D = 0.5$ without heat conduction in either direction, dimensionless (Eq. 1)
$(Q_D)_{TD=o.5}$ = cumulative heat injection at the breakthrough of $T_D = 0.5$ with heat conduction, dimensionless (Eq. 1)
T = temperature, °C
T_{inj}, T_{ini} = injection and initial temperature, °C
T_D = dimensionless temperature (Eq. 1)
t = cold-water injection time, s
t_{lj} = convection-driven thermal-front breakthrough time, s
t_{tj} = transverse thermal-conduction time across the two layers, s
u_j = Darcy velocity of cold-water injection, m/s
$\overline{v}$ = heat capacity-thickness weighted average convection velocity of the cooling-front in a two-layer system, m/s (Eq. 5)
v_j = convection velocity of the cooling front, m/s
W = reservoir width, m
x, y, z = Cartesian coordinates, m
x_D = dimensionless position in x direction (Eq. 1)
$\hat{x}_D$ = dimensionless position relative to a plane moving at $\overline{v}$(Eq. 15)
z_D = dimensionless position in z direction (Eq. 1)
α_{lj}, α_{tj} = longitudinal and transverse thermal diffusivity, m^2/s
$\bar{\alpha}_l$ = thickness-weighted average of longitudinal diffusivities α_{l1} and α_{l2}, m^2/s
α_{eff} = effective longitudinal thermal diffusivity, m^2/s (Eqs. 24 and 25)
κ_{lj}, κ_{tj} = longitudinal and transverse thermal conductivity, W/(m.K)
κ_{eff} = effective longitudinal thermal conductivity, W/(m.K)
$(\overline{\rho c_p})$ = thickness-weighted average heat capacity, J/(m^3.K) (Eq. 3)
$(\rho c_p)_j$ = layer heat capacity accounting for rock grains and fluids, J/(m^3.K) (Eq. 2)
$(\rho_w c_{pw})$ = heat capacity of water, J/(m^3.K)
$(\rho_{gj} c_{pgj})$ = heat capacity of rock grains, J/(m^3.K)
ϕ_j = porosity, dimensionless

References

Aris, R., 1956. On the dispersion of a solute in a fluid flowing through a tube. *Proceedings of the Royai Society of London. Series A. Mathematicai andPhysicai Sciences*, **235**(1200), 67–77.

Axelsson, G., Bjornsson, G., Montalvo, F., 2005. Quantitative interpretation of tracer test data. *in Proceedings Worid Geothermai Congress* (pp. 24–29).

Barton, N. G., 1983. On the method of moments for solute dispersion. *Journai of Fiuid Mechanics*, **126**, 205–218.

Batycky, R. P., Edwards, D. A., Brenner, H., 1994. Internal energy transport in adiabatic systems: Thermal Taylor dispersion phenomena. *Internationai Journai of Non-iinear Mechanics*, **29**(5), 639–664.

Berkowitz, B., Scher, H., 1996. Influence of embedded fractures on contaminant diffusion in geological formations. *Geophysicai Research Letters*, **23**(9), 925–928.

Bruderer, C., Bernabe, Y., 2001. Network modeling of dispersion: Transition from Taylor dispersion in homogeneous networks to mechanical dispersion in very heterogeneous ones. *Water Resources Research*, **37**(4), 897–908.

Bujakowski, W., Tomaszewska, B., Miecznik, M., 2016. The Podhale geothermal reservoir simulation for long-term sustainable production. *Renewabie Energy*, **99**, pp. 420–430.

Babaei, M., Nick, H. M., 2019. Performance of low-enthalpy geothermal systems: Interplay of spatially correlated heterogeneity and well-doublet spacings. *Applied Energy*, **253**, 113569.

Bredesen, K., Dalgaard, E., Mathiesen, A., Rasmussen, R., Balling, N., 2020. Seismic characterization of geothermal sedimentary reservoirs: A field example from the Copenhagen area, Denmark. *Interpretation*, **8**(2), T275–T291.

Blank, L., Meneses Rioseco, E., Caiazzo, A., Wilbrandt, U., 2021. Modeling, simulation, and optimization of geothermal energy production from hot sedimentary aquifers. *Computationai Geosciences*, **25**(1), 67–104.

Crooijmans, R. A., Willems, C. J., Nick, H. M., Bruhn, D. F., 2016. The influence of facies heterogeneity on the doublet performance in low-enthalpy geothermal sedimentary reservoirs. *Geothermics*, **64**, 209–219.

Detwiler, R. L., Rajaram, H., Glass, R. J., 2002. Experimental and simulated solute transport in a partially - saturated, variable-aperture fracture. *Geophysical Research Letters*, **29**(8), 113–1.

Dentz, M., Icardi, M., Hidalgo, J. J., 2017. Mechanisms of dispersion in a porous medium. arXiv Preprint arXiv:1709.07831.

Dejam, M., 2019. Advective-diffusive-reactive solute transport due to non-Newtonian fluid flows in a fracture surrounded by a tight porous medium. *International Journal of Heat and Mass Transfer*, **128**, 1307–1321.

Daniilidis, A., Nick, H. M., Bruhn, D. F., 2020. Interdependencies between physical, design and operational parameters for direct use geothermal heat in faulted hydrothermal reservoirs. *Geothermics*, **86**, 101806.

Emami Meybodi, H., Hassanzadeh, H., 2011. Hydrodynamic dispersion in steady buoyancy-driven geological flows. *Water Resources Research*, **47**(12).

Feng, G., Xu, T., Gherardi, F., Jiang, Z., Bellani, S., 2017. Geothermal assessment of the Pisa plain, Italy: Coupled thermal and hydraulic modeling. *Renewable Energy*, **111**, pp. 416–427.

Gringarten, A. C., 1978. Reservoir lifetime and heat recovery factor in geothermal aquifers used for urban heating. *Pure and Applied Geophysics*, **117**(1), 297–308.

Horne, R. N., Rodriguez, F., 1983. Dispersion in tracer flow in fractured geothermal systems. *Geophysical Research Letters*, **10**(4), 289292.

Hasan, A. R., Kabir, C. S., 1994. Aspects of wellbore heat transfer during two-phase flow (includes associated papers 30226 and 30970). *SPE Production & Facilities*, **9**(03), 211–216.

Hinton, E. M., Woods, A. W., 2020. Shear dispersion in a porous medium. Part 2. An intrusion with a growing shape. *Journal of Fluid Mechanics*, 899.

John, A. K., Lake, L. W., Bryant, S. L., Jennings, J. W., 2010. Investigation of mixing in field-scale miscible displacements using particle-tracking simulations of tracer floods with flow reversal. *Society of Petroleum Engineers Journal*, **15**(03), 598–609.

Kvernvold, O., Tyvand, P. A., 1980. Dispersion effects on thermal convection in porous media. *Journal of Fluid Mechanics*, **99**(4), 673686.

Khait, M., Voskov, D., 2018. Operator-based linearization for efficient modeling of geothermal processes. *Geothermics*, **74**, 7–18.

Lake, L. W., Hirasaki, G. J., 1981. Taylor's dispersion in stratified porous media. *Society of Petroleum Engineers Journal*, **21**(04), 459–468.

Lake, L., Johns, R. T., Rossen, W. R., Pope, G. A., 2014. Fundamentals of enhanced oil recovery. *Society of Petroleum Engineers*, Richardson, Texas.

Murphy, H. D., Tester, J. W., Grigsby, C. O., Potter, R. M., 1981. Energy extraction from fractured geothermal reservoirs in low- permeability crystalline rock. *Journal of Geophysical Research: Solid Earth*, **86**(B8), 7145–7158.

Nakayama, A., Kuwahara, F., Kodama, Y., 2006. An equation for thermal dispersion flux transport and its mathematical modelling for heat and fluid flow in a porous medium. *Journal of Fluid Mechanics*, **563**(1), 81–96.

Nissen, A., Keilegavlen, E., Sandve, T. H., Berre, I., Nordbotten, J. M., 2018. Heterogeneity preserving upscaling for heat transport in fractured geothermal reservoirs. *Computational Geosciences*, **22**(2), 451–467.

Nieuwkerk, P., 2022. Testing a thermal dispersion-based upscaling method for geothermal reservoir simulation. MSc thesis. Delft University of Technology.

Oldenburg, C. M., Pruess, K., 1998. Layered thermohaline convection in hypersaline geothermal systems. *Transport in Porous Media*, **33**(1), 29–63.

Ortan, A., Quenneville-Belair, V., Tilley, B. S., Townsend, J., 2009. On Taylor dispersion effects for transient solutions in geothermal heating systems. *International Journal of Heat and Mass Transfer*, **52**(21-22), 5072–5080.

Plumb, O. A., Whitaker, S., 1988. Dispersion in heterogeneous porous media: 1. Local volume averaging and large-scale averaging. *Water Resources Research*, **24**(7), 913–926.

Pearce, P., Daou, J., 2014. Taylor dispersion and thermal expansion effects on flame propagation in a narrow channel. *Journal of Fluid Mechanics*, **754**, 161.

Park, B. H., Lee, B. H., Lee, K. K., 2018. Experimental investigation of the thermal dispersion coefficient under forced groundwater flow for designing an optimal groundwater heat pump (GWHP) system. *Journal of hydrology*, **562**, 385–396.

Ramey, H. J., 1962. Wellbore heat transmission. *Journal of Petroleum Technology*, **14**(04), 427–435.

Rühaak, W., Guadagnini, A., Geiger, S., Bar, K., Gu, Y., Aretz, A., Homuth, S., Sass, I., 2015. Upscaling thermal conductivities of sedimentary formations for geothermal exploration. *Geothermics*, **58**, 49–61.

Seibert, S., Prommer, H., Siade, A., Harris, B., Trefry, M., Martin, M., 2014. Heat and mass transport during a groundwater replenishment trial in a highly heterogeneous aquifer. *Water Resources Research*, **50**(12), 9463–9483.

Shin, J., Seo, I. W., Baek, D., 2020. Longitudinal and transverse dispersion coefficients of 2D contaminant transport model for mixing analysis in open channels. *Journal of Hydrology*, **583**, 124302.

Taylor, G. I., 1953. Dispersion of soluble matter in solvent flowing slowly through a tube. *Proceedings of the Royal Society of London. Series A. Mathematical and Physical Sciences*, **219**(1137), 186–203.

Tang, D. W. S., van der Zee, S. E. A. T. M., 2021. Dispersion and recovery of solutes and heat under cyclic radial advection. *Journal of Hydrology*, **602**, 126713.

Vasilyeva, M., Babaei, M., Chung, E. T., Alekseev, V., 2019. Upscaling of the single-phase flow and heat transport in fractured geothermal reservoirs using nonlocal multicontinuum method. *Computational Geosciences*, **23**(4), 745–759.

Wikipedia, 2016. Taylor dispersion. Available at https://de.wikipedia.org/wiki/Taylor-Dispersion.

Willems, C. J., Nick, H. M., Weltje, G. J., Bruhn, D. F., 2017. An evaluation of interferences in heat production from low enthalpy geothermal doublets systems. *Energy*, **135**, 500–512.

Wang, Y., Voskov, D., Khait, M., Bruhn, D., 2020. An efficient numerical simulator for geothermal simulation: A benchmark study. *Applied Energy*, **264**, 114693.

Wang, Q., Shi, W., Zhan, H., Xiao, X., 2020. New model of single-well push-pull thermal test in a fracture-matrix system. *Journal of Hydrology*, **585**, 124807.

Wang, Y., Voskov, D., Khait, M., Saeid, S., Bruhn, D., 2021. Influential factors on the development of a low-enthalpy geothermal reservoir: A sensitivity study of a realistic field. *Renewable Energy*, **179**, pp. 641–651.

Yeo, I. W., Ge, S., 2001. Solute dispersion in rock fractures by Non-Darcian Flow. *Geophysical Research Lletters*, **28**(20), 3983–3986.

Yan, H., Xie, H., Nikolaev, P., Ding, H., Shi, Y., Chen, Y., 2022. Analytical model for steady-state solute diffusion in non-isothermal fractured porous media. *Journal of Hydrology*, 128872.